

# The KiHM-9: A Self-deploying PicoSat Holographic Metasurface Antenna (HMA) Design

Nathan M. Coleman<sup>\*1</sup>, Mitchel Skinner<sup>1</sup>, Collin Ynchausti<sup>1</sup>, Akash Biswas<sup>2</sup>, Constantinos L. Zekios<sup>2</sup>, Stavros V. Georgakopoulos<sup>2</sup>, Spencer P. Magleby<sup>1</sup>, and Larry L. Howell<sup>1</sup>

<sup>1</sup>Brigham Young University, Provo, UT

<sup>2</sup>Florida International University, Miami, FL

**A deployable holographic metasurface antenna design for small satellites is presented. The presented design uses an embedded membrane hinge that does not rely on adhesives, can be cycled repeatedly, and does not take up significant surface area away from the antenna. A novel stabilization method is also integrated which uses magnets for passive stabilization and is demonstrated to be notably flat in a micro-gravity simulated environment. Additionally, a compliant Euler spiral fold is used for integrated, low-profile deployment. The design is then validated using RF testing in an anechoic chamber, and the measured performance is shown to fulfill the expected nominal gain requirement.**

## I. Introduction

**T**HIS work addresses the popularity of smallsats by creating and demonstrating a novel holographic metasurface antenna (HMA) for smallsats that stows compactly, incorporates a unique surrogate hinge design, magnetic stabilization design, and deployment method. Trends in the aerospace industry have shown that the number of satellites launched into space each year has steadily increased for the last two decades [1]. One factor that has contributed to this trend is that technology has allowed satellites to become increasingly lighter and, therefore, less expensive to launch. An example of how satellites have become lighter is the advent of the CubeSat, which first launched in 2003 and has since become a standard platform for simple space missions [2–5]. CubeSats, along with other “PicoSats”, rely on antennas to establish radio transmission, as well as solar panels to power the satellite [6]. Because the performance of antennas and solar panels is directly related to their surface area, engineers have turned to various methods, including origami, to increase their ratio of deployed surface area to stowed volume [3, 7].

High-gain antennas such as parabolic reflectors, phased arrays (PAs), electronically steered arrays (ESAs), reflectarrays (RAs), transmitarrays (TAs), and metasurface antennas (MAs) are commonly used in satellite communication systems and each has its own advantages and disadvantages. For example, PAs can dynamically steer their beams in a desired direction with a high level of beam agility [8]; however, their designs are complex, and they require high-power beam-forming mechanisms that increase both their cost and their profile. TAs and RAs are simple, cost-effective solutions that achieve high gains due to their large apertures, but they have high profile due to the feed source placed several wavelengths away from the reflective surface\*

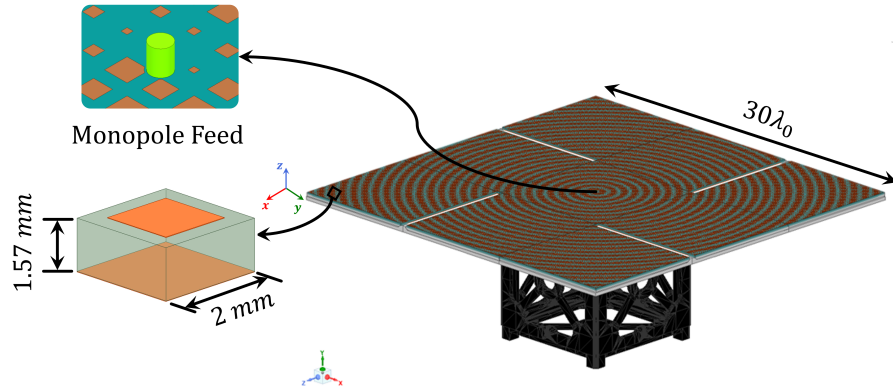
Metasurface antennas, particularly HMAs, have all the advantages of RAs and TAs, while, in addition, they are low-profile structures, making them promising candidates for use in satellite systems. Their performance is achieved using sub-wavelength unit cells (e.g., passive microstrip patch antennas of size  $\lambda/5 \times \lambda/5$  as shown in the bottom left inset of Fig. 1) properly distributed on their flat apertures, and fed by a single source placed at the center of the HMA’s aperture. Despite the attractive electromagnetic properties of all these large aperture high-gain antennas, folding them compactly for transport to space remains challenging. Stowed antennas must be deployed, which often requires peripheral infrastructure, significantly increasing the weight of the system. Due to these factors, reducing the weight of deployable antennas as well as reducing the weight of systems required to deploy the antennas is an important topic of research and focus of design.

Current satellites use a variety of methods to deploy and stabilize antennas, including telescoping booms [10–13], masts [14], exterior frames and trusses [15–17], stored strain energy in structures and tensioned cables [18–24],

---

\*Graduate Researcher, Mechanical Engineering, Compliant Mechanisms Research, Dept. of Mechanical Engineering, Brigham Young University, Provo, Utah 84602, ncolema4@byu.edu.

\*Notably, state-of-the-art reflectarrays with an aperture surface of  $58\lambda^2$ , designed to operate at 16 GHz for exhibiting the necessary realized gain of 26.4 dBi, place their feed antennas (e.g. horn antennas) at distance  $H_f = 9.4\lambda$  (where,  $\lambda = c/f$ ,  $f$  is the frequency of operation of the antenna and  $c$  is the speed of light) from the center of their apertures, that corresponds to 17.6cm,[9].

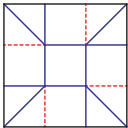
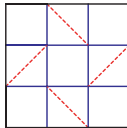
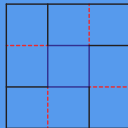
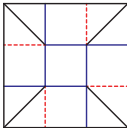


**Fig. 1** Initial deployed holographic metasurface antenna (HMA) concept design with 1U CubeSat structure. In the top left inset, the monopole that feeds the HMA is shown. In the bottom left inset, a 2mm sub-wavelength unit cell is shown consisting of a metallic square patch printed above a grounded substrate with a thickness of 1.57mm.

pneumatics [25, 26], and hardstops [27–31]. These techniques are viable solutions for maintaining the desired performance of antennas; however, some of these techniques require external structures, which occupy payload volume and add mass. These mechanisms are also dependent on hinges and bearings, which can be subject to friction and wear.

The objective of this work was to create an HMA that folds around the outside of a CubeSat and incorporates surrogate folds, a stabilization technique, and deployment methods (see Fig. 1). The pattern for this antenna was developed with zero-thickness origami models, which were then modified to accommodate the thickness of each panel. The final models considered are shown in Tab. 1, with the model chosen highlighted in blue.

**Table 1** Fold pattern candidates based on patterns that can fold around 1U CubeSats. The red dashed lines are valley folds, the blue solid lines are mountain folds, and the interior black solid lines are cuts. The selected pattern is highlighted in blue.

| Fold Pattern                    |  |  |  |  |
|---------------------------------|---|--|---|---|
| Fold Pattern Name               | Origami Box with Corner Folds   | Four-Sided Flasher   | Kirigami 9-Panel  | Kirigami 13-Panel   |
| Number of Folds                 | 16  | 16   | 8   | 12  |
| Mountain Folds                  | 12  | 12   | 4   | 8   |
| Valley Folds                    | 4   | 4  | 4   | 4   |
| Number of Cuts                  | 0   | 0  | 4   | 4   |
| Number of Folds and Cuts        | 16  | 16   | 12  | 16  |
| Rigid-Foldable                  | Yes   | No   | Yes   | Yes   |
| Special Thickness Accommodation | Yes   | Yes  | No  | No  |

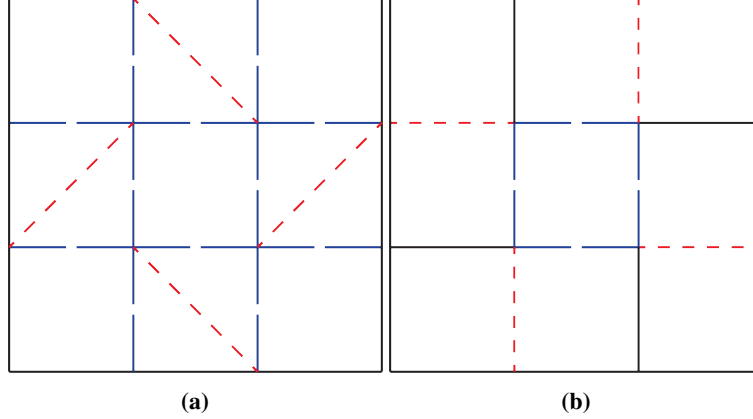


**Fig. 2** (a) Analog flasher pattern with parameters  $m=4$ ,  $r=1$ ,  $h=1$ , and  $dr=0$ . Each repeating quadrant is referred to as a “gore”. (b) Associated kirigami flasher pattern. Mountain folds are shown with blue long dashed lines, valley folds are shown with red short dashed lines, and cut lines are shown with black solid lines.

## II. Design

### A. Project Requirements

The aim of this work was to create a foldable metasurface that uses surrogate folds and other components appropriate for the space environment, can function reliably and repeatedly, deploys from a compact stowed area to a large deployed area, and is stable in a deployed configuration.

### B. Pattern Selection

The deployed shape and aspect ratio requirement was for the deployed antenna to fill out a square 9-panel metasurface and to stow compactly on the outer sides of the CubeSat. An example is shown in Fig. 1, which shows how the unfolded holographic metasurface antenna would work with a 1U CubeSat structure.

A kirigami flasher pattern was used for its simplicity and variety of folds. This pattern used a flasher pattern with the parameters  $m = 4$ ,  $r = 1$ ,  $h = 1$ , and  $dr = 0$  [32](shown in Fig. 2a), which was then modified to reduce the number of total panels and hinges by introducing cuts between gores, as shown in Fig. 2b. While modifying the design using kirigami principles introduces more degrees of the freedom to the flasher pattern, it was seen as desirable to reduce the complexity of integrating a pin-less hinge design by reducing the number of folds in the pattern, as well as reducing the number of panels that were manufactured from 13 to 9. Note that each repeating section of a flasher pattern is referred to as a “gore”, and so each of the four repeating sections in this design will also be referred to as such.

### C. Embedded Membrane surrogate folds

When origami patterns are thickened to accommodate materials, the paper folds must be replaced with “surrogate folds”. Often, this can be accomplished with a simple pin joint; however, this work sought to incorporate surrogate folds which are appropriate for a space environment and which would not require lubrication. An embedded membrane hinge was chosen for its ability to leave deployed panels on the same plane while maintaining a large usable surface area when deployed.

#### 1. Embedded Membrane Hinge Geometry

The embedded membrane hinge design chosen was developed by Ynchausti et al. [33]. This method uses two contacting circles of different radii to keep the membrane tensioned in both the open and closed positions, building off the Regionally Sandwiching of Compliant Sheets (ReCS) method of sandwiching a membrane between two panels. This modified approach increases control over the stress by varying the radius of the joint, allowing for less stress on the membrane while in a closed state, as shown in Fig. 3. When using this design, the larger radius,  $R_1$ , is the limiting factor for the total thickness of the final panels, which in turn determines the weight and volume of the overall antenna. As such,  $R_1$  was designed to be as small as possible, which was determined by the allowable stress in the membrane

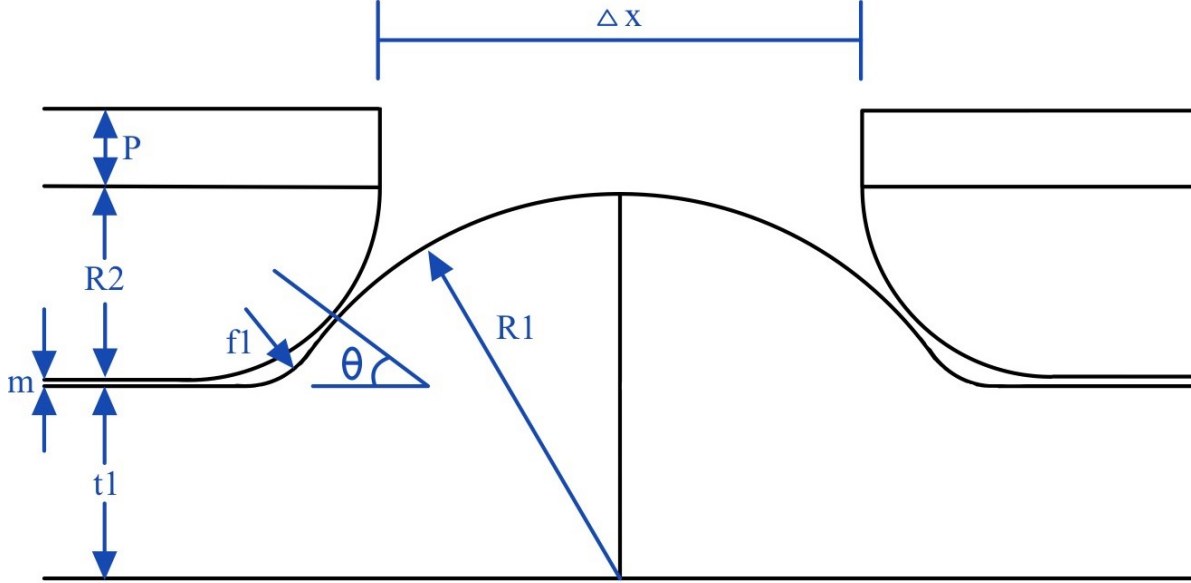


**Fig. 3 Geometry of hinge structure from Ynchausti et.al. [33]. Note that the thickness of the metasurface antenna panels is given by  $P$ , which is added to  $R_2$  to give  $R_{2, effective}$ .**

material. If the radius could be sufficiently thin, the limiting factor on the panel thickness would become the thickness required to achieve sufficient panel stiffness and limit compliance. The stress in the membrane hinge is given by

$$\sigma = \frac{Ec}{R} \quad (1)$$

which substituting  $\sigma = \frac{Mc}{I}$  into Eqn.(1), when solved for the required radius becomes

$$R \geq \frac{Em}{2S_y} \quad (2)$$

where  $R$  is the radius of the bend,  $E$  is the modulus of elasticity of the membrane material,  $m$  is the thickness of the membrane, and  $S_y$  is the yield strength of the membrane.

A stainless steel mesh was chosen as the hinge membrane material for its ability to maintain performance in constant exposure to UV radiation. The mesh used is a 306 Stainless Steel 400 mesh which was woven in a non-crimped pattern with a hole diameter of  $30 \mu\text{m}$  and a wire diameter of  $0.03 \text{ mm}$ . This mesh has a modulus of elasticity of  $E = 193 \text{ GPa}$ , a yield strength of  $S_y = 290 \text{ MPa}$ , and a thickness of  $h = 0.08 \text{ mm}$ . Note that in Fig. 3, the thickness of the PCB is added to  $R_2$  to give  $R_{2, effective}$ . When treating the mesh as a solid membrane and substituting these parameters into Eqn. (2), the radius required to avoid yielding of the material is found to be

$$R \geq 2.66 \text{ cm}. \quad (3)$$

This is a relatively large radius considering the scale of the antenna and mesh. However, because of the the nature of the mesh and how it is woven, it differed from a thin solid sheet which is assumed in the stress calculations. Here are a few factors that affect the stress of the stainless steel mesh:

- 1) The effective modulus of elasticity for a mesh of the same material would likely be different than that of a solid sheet.
- 2) Each wire in the mesh is not locked in place relative to the other wires around it, allowing it to more equally distribute loads within the mesh.
- 3) The total thickness of the mesh is greater than the thickness of any single wire being stressed, and so each wire can undergo more deflection before yielding than is predicted if it were the thickness of the mesh.
- 4) Due to the way the wires are woven over and under each other, the moment and stress applied to each wire are not equal to the moment applied to the mesh, and depend on the position of each wire in the weave. As such, Eqn. (2) is not a constant indicator of the actual maximum radius.

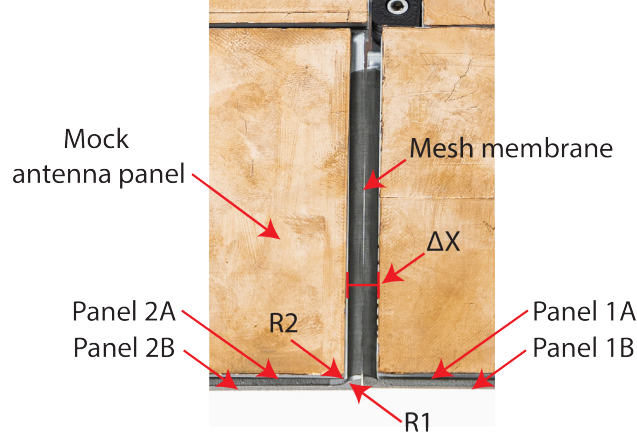


**Fig. 4 Close up of hinge design on final prototype.**

5) When one wire is stressed more than those around it, it can yield until the load is distributed to other wires, dispersing the load and prolonging time to failure due to one weak link.

Because of these considerations, Eqn. (3) can be taken to be an upper limit for  $R$ , and to account for these factors, a safety factor of 4 was used, resulting in a maximum radius of 0.5 cm, and this choice was verified through fatigue testing, detailed in Section III.A. The geometry of the radius on each panel complicated the manufacturing process and could be optimized in future work for each hinge material chosen. From a maximum radius of 0.5 cm, values are found for each variable, as listed in Table 2.

From these design values and using equations presented by Ynchausti et. al. [33] for the relationship between radii ( $R_1$ ,  $R_2$ ), the angle at which they are placed to each other ( $\theta$ ), and the total thickness ( $t_1$ ), are calculated as

$$\theta = \frac{\pi}{2} \left( \frac{R_2}{R_1 + R_2} \right) \quad (4)$$

$$t_1 = (R_1 + R_2) \cos(\theta) - R_2 \quad (5)$$

Because the PCB panels are relatively thin, and the mesh membrane thickness is negligible,  $R_{2, effective}$  becomes  $R_2 + P$ . This means that for this case  $\theta$  can be calculated as  $40.39^\circ$  and  $t_1 = 0.3995cm$ . With this design, the total surface area was  $900cm^2$ , with the hinges taking up just  $30cm^2$ , leaving  $870cm^2$  or 96.6% of the total area available. Fig. 4 shows the hinge design with the calculated geometry from Table 2 in the final prototype.

#### D. Stability with Magnetic Embedded Hinges

Magnets were selected for use in the stabilization method because of their ability to maintain a constant force over time without being subject to creep or stress relaxation. To keep a low profile, magnets were used in a simple bistable configuration with an offset inspired by Pruett et.al.[34]. Because there is an offset between magnets, the stability in the stowed state is minimal such that it takes a negligible force to overcome, making the configuration effectively

**Table 2 Geometric variables of designed hinge. Items with an asterisk were chosen, and not determined through calculation. Note that  $f_1$  is only necessary to facilitate manufacturing of the internal corner at the bottom  $R_1$ .**

| Variable           | Description                          | Value    |
|--------------------|--------------------------------------|----------|
| $R_1$              | Radius of the bottom panel           | 0.5 cm   |
| $R_2$              | Radius of the top panel              | 0.25 cm  |
| $f_1^*$            | Fillet radius                        | 0.2 cm   |
| $m^*$              | Membrane mesh thickness              | 0.008 cm |
| $P^*$              | Thickness of metasurface antenna PCB | 0.157 cm |
| $R_{2, Effective}$ | Effective R2                         | 0.407 cm |

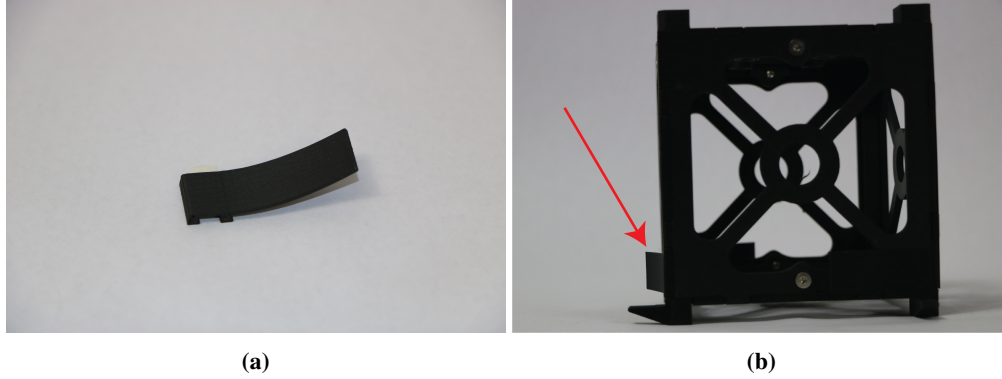


**Fig. 5 (a) Lenticular fold which folds completely flat when stowed and provides an opening force. (b) Side view of the lenticular fold showing its deployed position and displacement relative to a stowed flat position.**

monostable. Integrating this design in the kirigami flasher gains additional stability as the magnets in each gore interlock with the magnets in the two adjacent gores. Although the magnets could be much smaller in practice, as the antenna would not be subject to a constant gravitational force while in orbit, this model sought to demonstrate the effectiveness of a magnetic embedded hinge in achieving stability by supporting the full weight of the panels in the deployed state under Earth's gravity. To verify that the force of the magnets would be sufficient to support the antenna panels, magnets were put into an Instron tensile testing machine. The resulting forces found were then used to calculate that there would be a factor of safety for supporting the panels under earth's gravity of 1.3.

### E. Deployment

The flasher pattern, upon which the kirigami pattern is based, has one degree of freedom; however, by adding cuts, seven additional degrees of freedom were introduced.

As the degrees of freedom increase, so does the complexity of incorporating a deployment mechanism. Therefore, to reduce this complexity, an internal deployment system was preferred. Because magnets were already used for stabilization, they appeared to be an ideal method to use for deployment as well; however, the effective range of the magnetic force was insufficient when compared to the travel required by the panels over the course of their deployment. As such, a lenticular fold is integrated in the frame of the CubeSat to act as a spring during deployment.

#### 1. Lenticular Lock

The lenticular fold is a compliant mechanism that is manufactured in the shape of an Euler spiral, such that when deformed it stores strain energy and can lie flat. A deployable Euler spiral connector which was developed by Yellowhorse et al. [35] was integrated into each side of the CubeSat, as shown in Fig. 5. The lenticular fold is placed as far from the hinge as possible, to provide the largest moment arm to deploy the antenna panels. This functions such that the stowed state is an unstable state, and when a burn wire is cut the system will self-deploy. After 90° of motion the inner panels reach their hard stops, and the corner panels continue their motion due to their angular momentum.

## III. Prototypes and Testing

### A. Fatigue Testing

To validate the hinge membrane selected, the mechanics and fatigue life were first validated using 3D printed panels, after which the final design was created and tested using materials similar to those that would be used in space.

As shown in Section II.C.1, there are several unique factors that stem from using a woven mesh as the hinge membrane material as opposed to a uniform sheet material, each of which impact the calculated hinge radius needed to avoid yielding when bending, as given in Eqn. (2). Because of this, the calculated radius (Eqn. (3)) is taken to be an upper limit and not a design condition, and a smaller radius was chosen and validated using fatigue testing. Validation was particularly critical for the hinge system before it was integrated into the final design due to the difficulty of precisely predicting mesh performance. A  $R_1$  value of 0.5 cm was chosen and a  $R_2$  value of 0.25 cm was calculated, as shown in

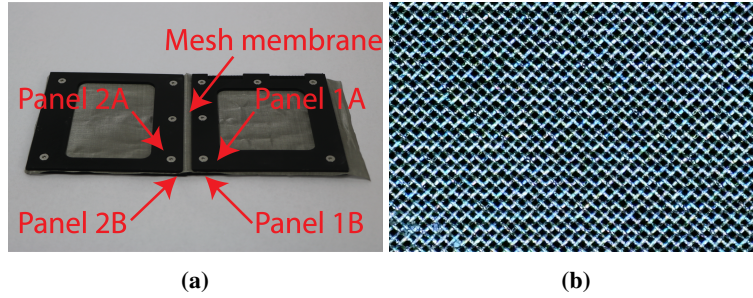


**Fig. 6** (a) Panels used to tension and fatigue test the stainless steel mesh hinge. (b) Close-up photograph from a microscope used to inspect the mesh for material wear and deformation, 50 times zoom, after 100 open-close cycles.

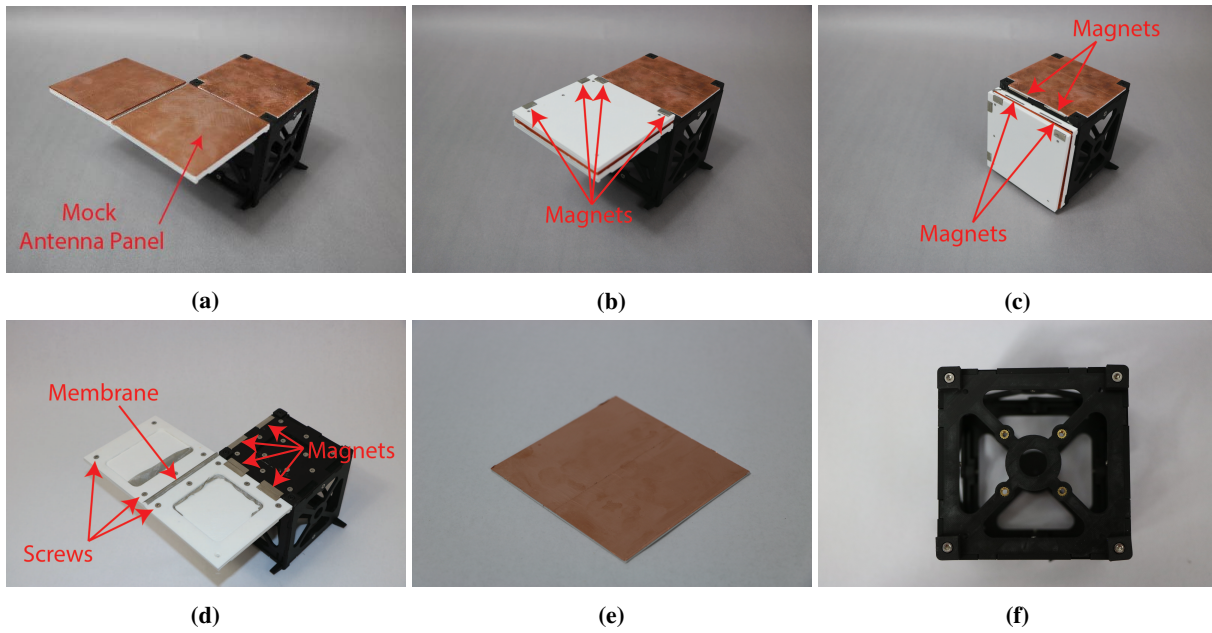


**Fig. 7** The initial CubeSat prototype with deployable antenna structure, shown with one of its four gores attached. (a) Deployed structure with mock antenna panels attached. (b) Mock panels half-closed. The smaller magnets used for stabilization between panels are shown. (c) Mock panels stowed. The larger magnets used for stabilization between each gore to the CubeSat are shown. Note that all panels except for the central top panel are covered and protected during stowage. (d) Deployed structure with mock antenna panels removed to show screw attachment locations. Note the cutout in each of the 1a and 2a (defined in Appendix I, Fig. 10) panels to reduce the weight of the overall structure as well as to tension the mesh during assembly. (e) Mock antenna panel with the same thickness as the proposed holographic metasurface antenna panels. (d) CubeSat attachment points on the top of the CubeSat. Threads are made with brass inserts in the 3D-printed CubeSat model.

Table 2.

To test this design, the stainless steel mesh was gripped between two panels and tensioned to 90 N (20 lbf). The joint was then manually cycled 100 times. This testing set-up is shown in Fig. 6. The results of this can be seen in Fig. 6 b, which shows a 50 times zoom of the mesh at the hinge location. Upon close inspection of the entire joint area, no mesh fibers were found to be broken, and no yielding of local wires could be found. Future work would improve this by testing and creating better models for various membrane hinge materials, so that the radius of the hinge could be more accurately optimized for a given application, resulting in thinner and lighter antennas.

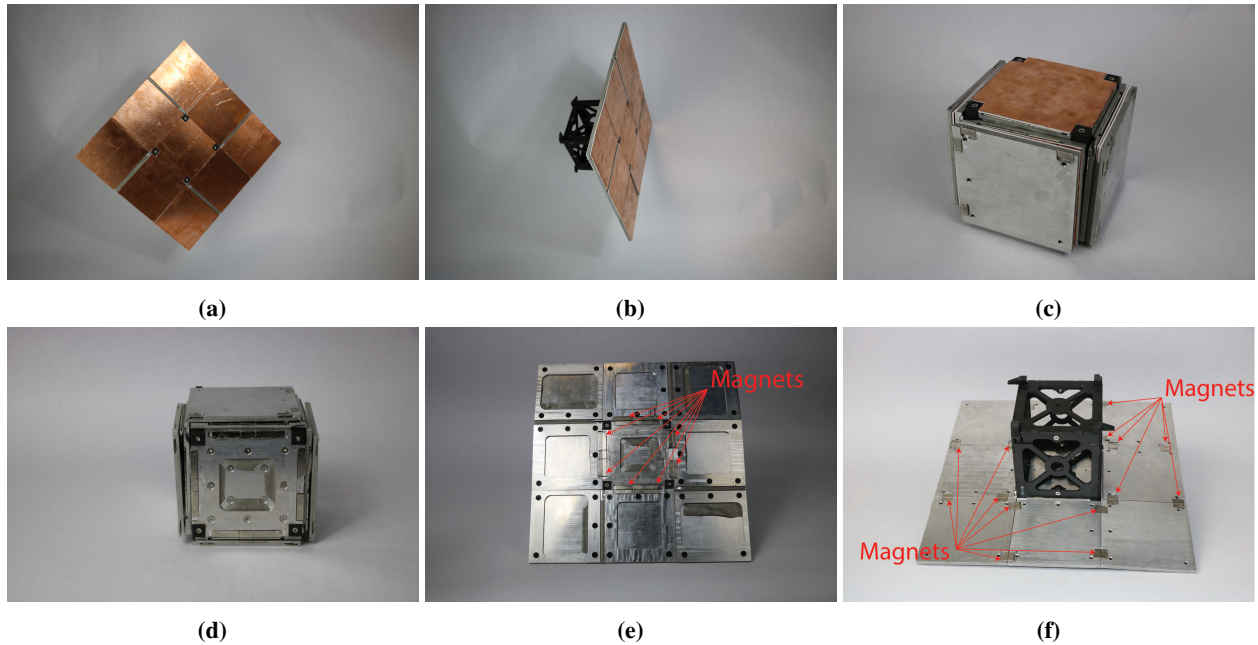


**Fig. 8** The final CubeSat prototype with deployable mock antenna panels shown with all four gores attached. (a) The structure in the deployed configuration, shows a full pattern with 9 mock antenna panels. Note the high area-use efficiency. (b) The structure in deployed configuration, side view. Note that in micro-gravity the mock antenna structure achieves remarkable flatness using the magnets for stabilization and panel thickness as hard stops. (c) Stowed structure. A burn wire would be used to delay deployment until desired, and all panels besides the central panel are covered until deployed. (d) The final structure with mock antenna panels removed, showing the top geometry holding the mesh in place and the magnet placement on the center panel. (e) Final structure with mock antenna panels removed showing the geometry of each panel in the pattern. (f) Bottom view of the final antenna showing magnet placement underneath each panel, which is used to interlock and stabilize each gore.

### B. Initial Prototype

A 3D printed model was created to verify design mechanics and behavior, as shown in Fig. 7. This model included mock antenna panels with the same thickness as actual panels to validate folding and stowage behaviors. This design also incorporated magnets to verify stabilization behavior.

### C. Manufacturing of Final Prototype

The deployable CubeSat prototype was designed to be as simple as possible, with uniformly shaped panels and common hardware used. The overall process used several manufacturing processes, including waterjet, CNC, and manual milling. Some manufacturing challenges that had to be overcome were the thinness of each panel, the varying radii in each panel, and the differing hole placement requirements between different panels. These factors required the use of three separate vacuum table setups, as well as three separate fixture plates. The manufacturing process is described in Appendix I, Table 3, and each part of the final antenna assembly can be found in the Bill of Materials in Appendix I, Table 4.

## IV. Results

### A. Final Model

Following assembly, the deployable structure was placed in a micro-gravity simulation, as shown in Fig. 8b. The flatness indicates that the magnetic hinges and hard stops were successful in stabilizing the deployable structure in the desired position and that the magnets used to interlock each gore to the next were effective in keeping each gore in the correct position relative to the gore next to it. There are several areas where future work could improve the results of



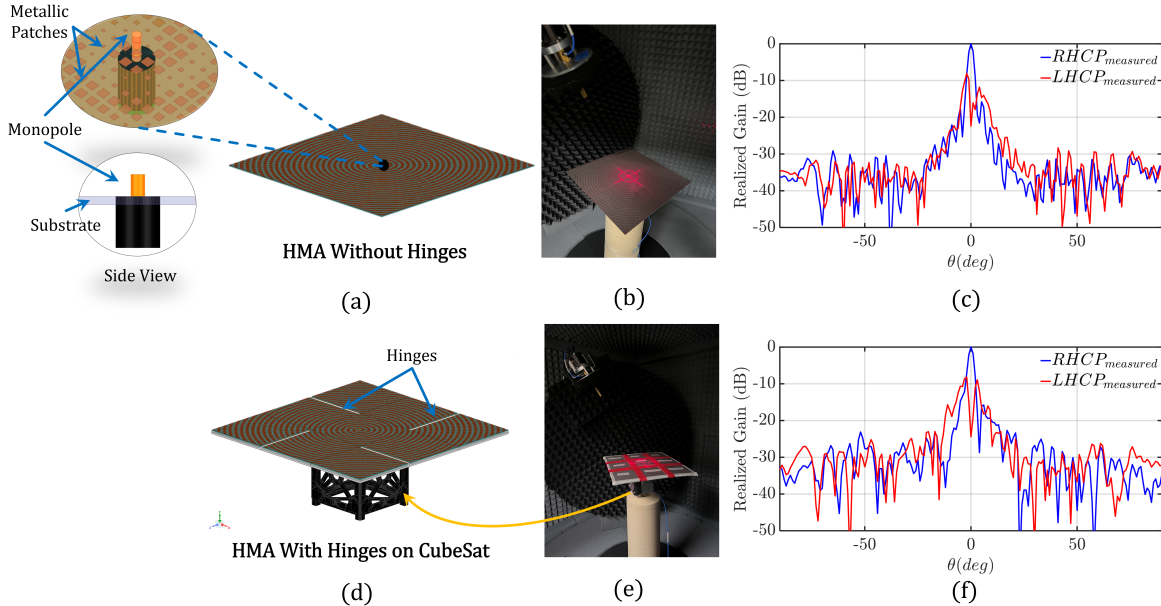


**Fig. 9** (a) A holographic metasurface antenna without hinges; At the inset, the monopole that feeds the HMA is shown in a zoomed view. (b) Measurement setup, and (c) 2-D normalized radiation pattern of the HMA prototype without hinges. (d) A fully deployed holographic metasurface antenna mounted on a CubeSat prototype. (e) Measurement setup, and (f) 2-D normalized radiation pattern of the fully deployed HMA prototype mounted on a CubeSat prototype.

this design. Epoxy was used to keep the magnets in place, and mechanical fasteners are recommended for future models for a more secure connection. Additionally, the mesh hinges, which were held in place by the clamping force of the top and bottom panels, were noted to slip when left for extended periods of time, which would not be an issue in the zero-gravity environment of space, but which is nonetheless an undesired behavior, and could be reduced by using epoxy in addition to the clamping force, to further secure the mesh within the panels. The antenna panels could also be made using forged carbon fiber, which may allow for easier manufacturing of the panel radii and production at scale.

## B. RF Testing

Once the mechanical performance was validated, the mock antenna panels were replaced with the final holographic metasurface antenna (HMA) prototype. In turn, the performance of the HMA was evaluated through design in ANSYS HFSS and prototype measurements in a standard anechoic chamber. Notably, two HMA designs of electrical size  $30\lambda \times 30\lambda$  were modeled<sup>†</sup>, fabricated and measured; (a) an HMA design with no hinges (see Fig. 9a) that was used as a reference, and (b) a foldable HMA design comprised of 9 separate panels and 4 rectangular cuts of size  $\Delta x = 5.5$  mm properly designed to accommodate the area of the hinges designed in Section II.C.1 (see Figs. 3 and 9d). Aiming towards a circularly polarized broadside beam which is essential in satellite communications, a concentric circle-based holographic pattern was properly designed, as depicted in Fig. 9a. To feed the HMA, a monopole antenna was used, placed at the center of the radiating aperture and powered by a coaxial cable connected at the back side of the panel (see inset of Fig. 9a).

Figures 9b and 9e shows two fabricated prototypes placed inside a MVG MicroLab anechoic chamber [36], while Figs. 9c and 9f show the corresponding measured normalized 2-D realized gains. Notably, the HMA without the hinges achieved a total realized gain of 30 dBi, while the deployed HMA achieved 27 dBi. The 3 dB difference between these results is attributed to fabrication errors, and alignment imperfections when the HMA panels were placed on the deployable structure assembled on the CubeSat. Nevertheless, the gain of 27 dBi fulfills the required nominal gain for establishing reliable communication between a terrestrial base station and a CubeSat.

<sup>†</sup> Both HMA designs were designed to operate at  $f = 30$  GHz;  $\lambda = c/f$ ,  $c = 3 \times 10^8$  m/s

## V. Conclusion

The design and manufacture of the KiHM-9 antenna demonstrates the effectiveness and potential of using various novel technologies, as well as using origami as a starting point for pattern selection. This design validated the performance of magnetic embedded hinges as a method of stabilizing a deployable array without the need for active elements. It also demonstrated the feasibility of embedded membrane hinges as surrogates for zero-thickness models and discusses ways that they might improve in the future. RF testing of the final prototype showed an acceptable level of gain when compared to the simulated results, further validating the capability of the technologies. These technologies combined serve to reduce the peripherals required for deployment and stabilization.

The KiHM-9 shows the potential for future work in this area. Several areas of profitable research for the future stemming from this work are optimizing the hinge radius on the embedded membrane hinge design used by creating better stress and fatigue models for materials used in membrane hinges and exploring different manufacturing methods and materials for the radius hinge design. Additionally, future work could benefit by experimenting with other methods of securing components, such as adding epoxy to keep the mesh membrane from slipping when stowed and mechanically securing the magnets rather than relying solely on adhesives. Other methods of manufacturing could be explored to facilitate the production of the different radii in the hinge design.

By following the methodology laid out in this work and employing the technologies shown herein, designers can create self-deploying and self-stabilizing space-based holographic metasurface antennas.

## Appendix I

**Table 3 Manufacturing Steps.**

| Step | Part                    | Operation                | Manufacturing Method   |
|------|-------------------------|--------------------------|------------------------|
| 1    | All panels              | Cut out profile          | Waterjet               |
| 2    | Vacuum plate            | Mill                     | CNC                    |
| 3    | All fixture plates      | Mill                     | CNC                    |
| 4    | All panels, top side    | Mill                     | CNC with vacuum plate  |
| 5    | All panels, bottom side | Mill                     | CNC with fixture plate |
| 6    | Stainless steel mesh    | Cut                      | Scissors               |
| 7    | Magnet                  | Attach                   | Epoxy                  |
| 8    | All gores               | Connect panels           | Screw together         |
| 9    | All gores               | Connect to central panel | Screw together         |
| 10   | Antenna                 | Connect to CubeSat       | Screw together         |

**Table 4 Bill of Materials. See Appendix I, Fig. 10 for nomenclature on panel numbering.**

| Part                                   | Quantity | Attachment Method |
|--|----------|-------------------|
| Panel 0A                               | 1        | Screws            |
| Panel 0B                               | 1        | Screws            |
| Panel 1A                               | 4        | Screws            |
| Panel 1B                               | 4        | Screws            |
| Panel 2A                               | 4        | Screws            |
| Panel 2B                               | 4        | Screws            |
| 1" by 1/4" by 1/16" Neodymium Magnet   | 8        | Epoxy             |
| 1/2" by 1/4" by 1/16" Neodymium Magnet | 32       | Epoxy             |
| M3x5mm Flat Head Machine Screws        | 4        | N/A               |
| M4x5mm Flat Head Machine Screws        | 52       | N/A               |
| 316 Stainless Steel 400 Mesh           | 1        | Friction          |

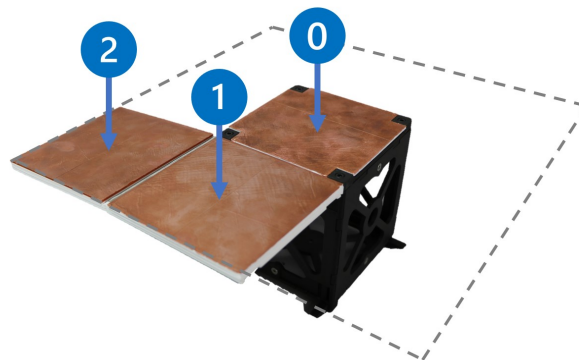


**Fig. 10** Numbering nomenclature of the panels during manufacturing. Note that “a” refers the top half of the panel (associated with  $R_2$  on panels 1 and 2) and “b” refers to the bottom half of the panel (associated with  $R_1$  on panels 1 and 2).

### **Acknowledgements**

This work has been funded by the Air Force Research Lab/U.S. Space Force, through award number FA9453-22-C-0013, and is also based on work supported by the Air Force Office of Scientific Research grant FA9550-19-1-0290 through Florida International University. Additional acknowledgment and thanks are given to the Utah NASA Space Grant Consortium that made this work possible.

Special thanks and acknowledgement are given to BYU Prototyping Lab assistants Camilla Cave and Ethan Hall, who machined the final antenna panels for this work.

## References

- [1] Salas, E. B., “Number of satellites launched by year 2019,” Mar 2022. URL <https://www.statista.com/statistics/896699/number-of-satellites-launched-by-year/>.
- [2] Toorian, A., Diaz, K., and Lee, S., “The CubeSat Approach to Space Access,” *IEEE Xplore*, 2008, pp. 1–14. <https://doi.org/10.1109/AERO.2008.4526293>.
- [3] Rahmat-Samii, Y., Manohar, V., and Kovitz, J. M., “For Satellites, Think Small, Dream Big: A review of recent antenna developments for CubeSats.” *IEEE Antennas and Propagation Magazine*, Vol. 59, No. 2, 2017, pp. 22–30.
- [4] Lokman, A. H., Soh, P. J., Azemi, S. N., Lago, H., Podilchak, S. K., Chalermwisutkul, S., Jamlos, M. F., Al-Hadi, A. A., Akkaraekthalin, P., and Gao, S., “A review of antennas for picosatellite applications,” *International Journal of Antennas and Propagation*, Vol. 2017, 2017.
- [5] Liu, Z.-Q., Qiu, H., Li, X., and Yang, S.-L., “Review of large spacecraft deployable membrane antenna structures,” *Chinese Journal of Mechanical Engineering*, Vol. 30, No. 6, 2017, pp. 1447–1459.
- [6] Chahat, N., Hodges, R. E., Sauder, J., Thomson, M., and Rahmat-Samii, Y., “The Deep-Space Network Telecommunication CubeSat Antenna: Using the deployable Ka-band mesh reflector antenna.” *IEEE Antennas and Propagation Magazine*, Vol. 59, No. 2, 2017, pp. 31–38. <https://doi.org/10.1109/MAP.2017.2655576>.
- [7] Kaddour, A.-S., Velez, C. A., Hamza, M., Brown, N. C., Ynchausti, C., Magleby, S. P., Howell, L. L., and Georgakopoulos, S. V., “A Foldable and Reconfigurable Monolithic Reflectarray for Space Applications,” *IEEE Access*, Vol. 8, 2020, pp. 219355–219366.
- [8] Mailloux, R. J., “Phased Array Antenna Handbook, Third Edition,” *Artech House*, 2017.
- [9] Rubio, A. J., Kaddour, A.-S., Ynchausti, C., Magleby, S., Howell, L. L., and Georgakopoulos, S. V., “A Foldable Reflectarray on a Hexagonal Twist Origami Structure,” *IEEE Open Journal of Antennas and Propagation*, Vol. 2, 2021, pp. 1108–1119. <https://doi.org/10.1109/OJAP.2021.3127312>.
- [10] McEachen, M. E., *Compact Telescoping Array: Advancement from Concept to Reality*, AIAA, 2018, Chap. 1, p. 1. <https://doi.org/10.2514/6.2018-1945>, URL <https://arc.aiaa.org/doi/abs/10.2514/6.2018-1945>.
- [11] Leclerc, C., Wilson, L. L., Bessa, M. A., and Pellegrino, S., *Characterization of Ultra-Thin Composite Triangular Rollable and Collapsible Booms*, AIAA, 2017, Chap. 1, p. 1. <https://doi.org/10.2514/6.2017-0172>, URL <https://arc.aiaa.org/doi/abs/10.2514/6.2017-0172>.
- [12] Firth, J. A., and Pankow, M. R., “Advanced Dual-Pull Mechanism for Deployable Spacecraft Booms,” *Journal of Spacecraft and Rockets*, Vol. 56, No. 2, 2019, pp. 569–576. <https://doi.org/10.2514/1.A34243>, URL <https://doi.org/10.2514/1.A34243>.
- [13] Block, J., Straubel, M., and Wiedemann, M., “Ultralight deployable booms for solar sails and other large gossamer structures in space,” *Acta Astronautica*, Vol. 68, No. 7, 2011, pp. 984–992. <https://doi.org/https://doi.org/10.1016/j.actaastro.2010.09.005>, URL <https://www.sciencedirect.com/science/article/pii/S0094576510003437>.
- [14] Guoa, H., Liu, R., Deng, Z., and Zhang, J., “Dynamic Characteristic Analysis of Large Space Deployable Articulated Mast,” *Procedia Engineering*, Vol. 16, 2011, pp. 716–722. <https://doi.org/https://doi.org/10.1016/j.proeng.2011.08.1146>, URL <https://www.sciencedirect.com/science/article/pii/S1877705811026476>, international Workshop on Automobile, Power and Energy Engineering.
- [15] Greschik, G., Mejia-Ariza, J. M., Murphey, T. M., and Jeon, S. K., “Error Suppression via Tension for Flexible Square Antenna Panels and Panel Arrays,” *AIAA Journal*, Vol. 53, No. 3, 2015, pp. 513–531. <https://doi.org/10.2514/1.J052691>, URL <https://doi.org/10.2514/1.J052691>.
- [16] Tamura, A., Inoue, S., Kawarabayashi, D., Yamazaki, M., and Miyazaki, Y., *Deployment Dynamics of Self-deployable Truss Structure Consisting of Bi-convex Booms*, AIAA, 2017, Chap. 1, p. 1. <https://doi.org/10.2514/6.2017-0175>, URL <https://arc.aiaa.org/doi/abs/10.2514/6.2017-0175>.
- [17] Webb, D., Hirsch, B., Bach, V., Sauder, J., Bradford, S., and Thomson, M., “Starshade Mechanical Architecture & Technology Effort,” *3rd AIAA Spacecraft Structures Conference*, AIAA, 2016, p. 1. <https://doi.org/10.2514/6.2016-2165>.
- [18] Chilan, C. M., Herber, D. R., Nakka, Y. K., Chung, S.-J., Allison, J. T., Aldrich, J. B., and Alvarez-Salazar, O. S., “Co-Design of Strain-Actuated Solar Arrays for Spacecraft Precision Pointing and Jitter Reduction,” *AIAA Journal*, Vol. 55, No. 9, 2017, pp. 3180–3195. <https://doi.org/10.2514/1.J055748>, URL <https://doi.org/10.2514/1.J055748>.

- [19] Pehrson, N. A., Smith, S. P., Ames, D. C., Magleby, S. P., and Arya, M., *Self-Deployable, Self-Stiffening, and Retractable Origami-Based Arrays for Spacecraft*, AIAA, 2019, Chap. 1, p. 1. <https://doi.org/10.2514/6.2019-0484>, URL <https://arc.aiaa.org/doi/abs/10.2514/6.2019-0484>.
- [20] Chu, Z., Deng, Z., Qi, X., and Li, B., “Modeling and analysis of a large deployable antenna structure,” *Acta Astronautica*, Vol. 95, 2014, pp. 51–60. <https://doi.org/https://doi.org/10.1016/j.actaastro.2013.10.015>, URL <https://www.sciencedirect.com/science/article/pii/S0094576513003858>.
- [21] Crawford, R., Hedgepeth, J., and Preiswerk, P., *Spoked wheels to deploy large surfaces in space*, AIAA, 2012, Chap. 1, p. 1. <https://doi.org/10.2514/6.1974-1267>, URL <https://arc.aiaa.org/doi/abs/10.2514/6.1974-1267>.
- [22] Qi, X., Huang, H., Li, B., and Deng, Z., “A large ring deployable mechanism for space satellite antenna,” *Aerospace Science and Technology*, Vol. 58, 2016, pp. 498–510. <https://doi.org/https://doi.org/10.1016/j.ast.2016.09.014>, URL <https://www.sciencedirect.com/science/article/pii/S127096381630671X>.
- [23] Dong, S., and Yuan, X., “Pretension process analysis of prestressed space grid structures,” *Journal of Constructional Steel Research*, Vol. 63, 2007, pp. 406–411. <https://doi.org/10.1016/j.jcsr.2006.04.006>.
- [24] Luo, M., Yan, R., Wan, Z., Qin, Y., Santoso, J., Skorina, E. H., and Onal, C. D., “OriSnake: Design, Fabrication, and Experimental Analysis of a 3-D Origami Snake Robot,” *IEEE Robotics and Automation Letters*, Vol. 3, No. 3, 2018, pp. 1993–1999. <https://doi.org/10.1109/LRA.2018.2800112>.
- [25] Ranzani, T., Russo, S., Schwab, F., Walsh, C. J., and Wood, R. J., “Deployable stabilization mechanisms for endoscopic procedures,” *2017 IEEE International Conference on Robotics and Automation (ICRA)*, 2017, pp. 1125–1131. <https://doi.org/10.1109/ICRA.2017.7989134>.
- [26] Zirbel, S., Magleby, S., Trease, B., and Howell, L., *The 42nd Aerospace Mechanism Symposium*, NASA, 2014, Chap. 1, p. 1. URL <http://www.esmats.eu/amspapers/pastpapers/pdfs/2014/zirbel.pdf>.
- [27] Blandino, J. R., Ross, B., Woo, N., Smith, Z., and McNaul, E., *Simulating CubeSat Structure Deployment Dynamics*, AIAA, 2018, Chap. 1, p. 1. <https://doi.org/10.2514/6.2018-1677>, URL <https://arc.aiaa.org/doi/abs/10.2514/6.2018-1677>.
- [28] Fang, H., Li, S., and Wang, K. W., “Self-locking degree-4 vertex origami structures,” *Proceedings of the Royal Society A: Mathematical, Physical and Engineering Sciences*, Vol. 472, No. 2195, 2016, p. 20160682. <https://doi.org/10.1098/rspa.2016.0682>.
- [29] Filipov, E. T., Tachi, T., and Paulino, G. H., “Origami tubes assembled into stiff, yet reconfigurable structures and metamaterials,” *Proceedings of the National Academy of Sciences*, Vol. 112, No. 40, 2015, pp. 12321–12326. <https://doi.org/10.1073/pnas.1509465112>, URL <https://www.pnas.org/doi/abs/10.1073/pnas.1509465112>.
- [30] Gattas, J., and You, Z., “Geometric assembly of rigid-foldable morphing sandwich structures,” *Engineering Structures*, Vol. 94, 2015, pp. 149–159. <https://doi.org/https://doi.org/10.1016/j.engstruct.2015.03.019>, URL <https://www.sciencedirect.com/science/article/pii/S0141029615001558>.
- [31] Shemanski, P., and Trease, B., “Compact Directional and Frictional Hinges for Flat Folding Applications,” *ASME*, 2018, p. V05BT07A064. <https://doi.org/10.1115/DETC2018-86225>.
- [32] Lang, R. J., Tolman, K. A., Crampton, E. B., Magleby, S. P., and Howell, L. L., “A review of thickness-accommodation techniques in origami-inspired engineering,” *Applied Mechanics Reviews*, Vol. 70, No. 1, 2018.
- [33] Ynchausti, C., Shirley, S., Magleby, S. P., and Howell, L. L., “Adjustable, Radii-Controlled Embedded Lamina (RadiCEL) Hinges for Folding of Thick Origami-Adapted Systems,” *Mechanism and Machine Theory*, 2023. In Review.
- [34] Pruett, H., Coleman, N., and Magleby, S. P., “Preliminary Concepts for Magnetic Actuation and Stabilization of Origami-Based Arrays,” *International Design Engineering Technical Conferences and Computers and Information in Engineering Conference*, Vol. 1, American Society of Mechanical Engineers (in review), 2022, p. 1.
- [35] Yellowhorse, A., and Howell, L. L., “Deployable lenticular stiffeners for origami-inspired mechanisms,” *Mechanics Based Design of Structures and Machines*, Vol. 46, No. 5, 2018, pp. 634–649.
- [36] <https://www.mvg-world.com>, 2023. Accessed: May 2023.